Ferroelectric domains in epitaxial $Pb_xSr_{1-x}TiO_3$ thin films investigated using X-ray diffraction and piezoresponse force microscopy

S. Fernandez-Peña' , C. Lichtensteiger, P. Zubko, C. Weymann, S. Gariglio, and J.-M. Triscone

Citation: APL Mater. **4**, 086105 (2016); doi: 10.1063/1.4960621
View online: http://dx.doi.org/10.1063/1.4960621
View Table of Contents: http://aip.scitation.org/toc/apm/4/8
Published by the American Institute of Physics

Ferroelectric domains in epitaxial $Pb_xSr_{1-x}TiO_3$ thin films investigated using X-ray diffraction and piezoresponse force microscopy

S. Fernandez-Peña,[1,a] C. Lichtensteiger,[1] P. Zubko,[2] C. Weymann,[1]
S. Gariglio,[1] and J.-M. Triscone[1]
[1]*DQMP, University of Geneva, 24 Quai E. Ansermet, 1211 Geneva 4, Switzerland*
[2]*London Centre for Nanotechnology and Department of Physics and Astronomy, University College London, 17–19 Gordon Street, London WC1H 0HA, United Kingdom*

(Received 16 June 2016; accepted 21 July 2016; published online 10 August 2016)

We present a detailed study of compressively strained $Pb_xSr_{1-x}TiO_3$ thin films grown by off-axis radio frequency magnetron sputtering on (001)-oriented Nb-doped $SrTiO_3$ substrates. Film tetragonality and the ferroelectric critical temperatures are measured for samples of different composition and thickness and compared with a phenomenological Landau-Devonshire model. 180° ferroelectric domains are observed using both X-ray diffraction and piezoresponse force microscopy and domain sizes obtained by the two techniques are compared and discussed.
[http://dx.doi.org/10.1063/1.4960621]

Over the last decade, $PbTiO_3$ thin films have served as a model system for studies of ferroelectricity in the ultrathin limit and the instability of the spontaneous polarization to nanoscale domain formation. The functional properties of such films are strongly influenced by depolarizing fields that arise from the imperfect screening of the ferroelectric polarization. These fields are minimized by the appearance of 180° stripe domains. The observation of such domains for instance in $PbTiO_3$ films as thin as 3 unit cells[1,2] has motivated numerous studies aimed at understanding and controlling the electrostatic boundary conditions that lead to domain formation, as well as the effect such domains have on the functional properties of ferroelectric thin films. For example, the effects of screening on domain formation were studied for samples with different electrodes,[1,3,4] dielectric spacers,[5,6] and ionic adsorbates.[7,8] Photochemical switching of stripe domains was reported by Takahashi *et al.* in Ref. 9, whereas Ref. 10 investigated the possibility of polarization switching without domain formation in ultrathin films near the ferroelectric critical temperature T_C. More complex $PbTiO_3$-based heterostructures, such as ferroelectric-dielectric ($PbTiO_3$-$SrTiO_3$) superlattices,[11–14] have been particularly useful for investigating the response of nanoscale stripe domains to applied fields and their effect on the macroscopic electrical properties.[15,16] In addition, many theoretical studies have addressed the formation and microscopic and macroscopic properties of nanoscale stripe domains, revealing complex, inhomogeneous polarization profiles,[17–20] and unusual switching dynamics.[21–23]

The small domain sizes, which scale according to the Landau-Lifshitz-Kittel law as the square root of the film thickness,[24] make local imaging of the domain structure by piezoresponse force microscopy (PFM) challenging for films thinner than ~10 nm[6,25] and thus information on nanoscale domains is usually obtained using X-ray diffraction (XRD). Only within a narrow range of domain sizes can both techniques be applied, as reported here, providing a valuable cross-check between these real and reciprocal space methods.[6,25]

[a]Electronic mail: stephanie.fernandez@unige.ch

In this work, we investigate the 180° domain structure of thin films of Sr-substituted $PbTiO_3$ or $Pb_xSr_{1-x}TiO_3$ (PST). Compared with other solid solutions containing PTO, most notably $Pb(Zr_xTi_{1-x})O_3$ (PZT), which are technologically important because of their superior electrical and electromechanical properties, PST has received much less attention due to its simpler phase diagram that lacks the morphotropic phase boundary of PZT. Bulk PST exhibits a single phase transition from a high temperature cubic (paraelectric) phase to a low-temperature tetragonal (ferroelectric) phase[26–28] with a transition temperature that increases linearly with Pb content.[29] On the other hand, in thin films, epitaxial strain can be used to induce new phases[30] as well as to control the ferroelastic domain structure.[31]

We study compressively strained thin films of PST grown on (001) Nb-doped $SrTiO_3$ (Nb:STO) substrates. We focus on a set of PST thin films with different compositions and bottom electrodes allowing the degree of screening of the polarization to be changed. The tetragonality and T_C of PST for different compositions are studied using temperature dependent XRD and compared to the predictions of Landau-Devonshire theory, whereas the ferroelectric domain structure is studied using a combination of XRD and PFM allowing the domain sizes to be quantified. The results obtained using these two techniques are compared.

The samples were grown by radio-frequency off-axis magnetron sputtering on (001)-oriented Nb-doped (0.5 wt. %) STO substrates with and without an *ex situ* sputtered 15-unit-cell-thick $LaNiO_3$ (LNO) buffer layer. Optimal growth conditions can be found in Refs. 32 and 56. Sub-monolayer fractions of each material (STO and PTO) were grown alternately to achieve the target composition of $Pb_xSr_{1-x}TiO_3$ with x varying from 0 to 1. We note that this deposition method may not result in a true random alloy as there may be some clustering of PTO and STO within any particular monolayer. Any clusters, however, are likely to be randomly arranged along the out-of-plane direction from one monolayer to the next and no evidence of cation ordering along the growth direction is observed from the XRD data. Thus, electrostatically, such films should be a good approximation to a true solid solution.[12] In order to control the composition, the STO and PTO deposition rates were carefully pre-calibrated. Rutherford backscattering measurements were performed on two representative samples to confirm the Pb/Sr ratio. Samples with intended compositions $x = 0.6$ and $x = 0.4$ were found to have $x = 0.605 \pm 0.006$ and $x = 0.455 \pm 0.005$, respectively. This deviation from the intended composition is indicated by the error bar in Fig. 1(b) for $x = 0.4$. Fig. 1(a) shows the XRD intensity around the (001) reflections for 60-nm-thick samples of different compositions. The measurements were performed with a PANalytical X'Pert Pro diffractometer equipped with a monochromator and a triple axis detector. The finite size oscillations attest to the high crystalline quality of the thin films and maps of the reciprocal space around the $(\bar{1}03)$ reflections confirmed that all the layers were fully strained to the substrate (not shown here).

In order to obtain accurate values for the out-of-plane lattice parameter c, the XRD data were simulated with a model described in Ref. 33. The diffraction measurements were then performed

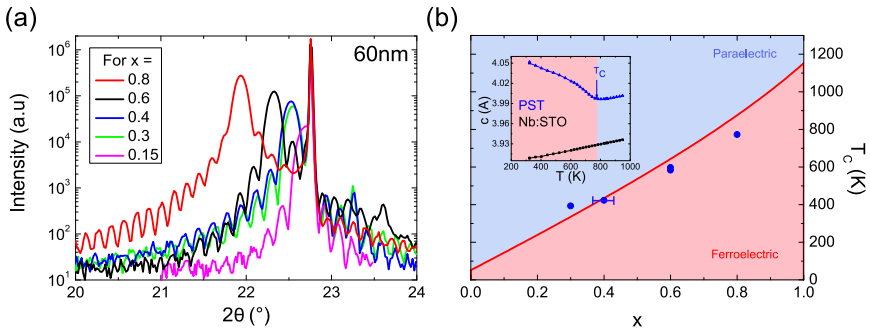

FIG. 1. (a) XRD θ-2θ diffractograms for ~60 nm thick samples with different compositions grown on Nb:STO showing the (001) PST reflections. The increase in intensity for the layer peak is due to the larger content of the heavier Pb atoms. (b) T_C for different x: the blue points are the experimental data, whereas the red line is the result of the LD calculation. The inset represents the c-axis evolution of the substrate and of the film as a function of temperature; the T_C is defined by the kink (data for a 63 nm thick film with $x = 0.8$).

as a function of temperature in order to follow the evolution of the lattice parameters across the ferroelectric-paraelectric phase transition. A typical result is shown in the inset of Fig. 1(b). In the ferroelectric phase, the *c*-axis lattice parameter decreases upon heating as the polarization decreases. By contrast, in the paraelectric phase, at high temperature, the *c* lattice parameter increases as the film undergoes thermal expansion. The point at which this change in behavior is observed is taken as T_C, as is common practice.[11,34,35] The Curie temperatures obtained by analyzing the temperature evolution of the most intense (002) diffraction peak are plotted as a function of x in Fig. 1(b).

To model the behavior of the alloy we have used Landau-Devonshire (LD) theory assuming the PST film to have a homogeneous polarization (i.e., neglecting domains and depolarization fields) and an in-plane lattice constant equal to that of the Nb:STO substrate (3.905 Å).[36–38] The misfit strain $S_x = \frac{a_{sub}-a_0}{a_0}$ is defined in terms of the in-plane lattice constant of the film, equal to that of the substrate a_{sub}, and the equivalent cubic lattice constant of the free standing film a_0. The model is essentially the same as that previously developed for PTO-STO superlattices in Ref. 11. The energy functional is given by

$$F = \alpha_1^* P_z^2 + \alpha_{11}^* P_z^4 + \alpha_{111} P_z^6 + S_x^2 \frac{c_{11}^2 + c_{12}c_{11} - 2c_{12}^2}{c_{11}}, \tag{1}$$

where α_1^* and α_{11}^* are the strain-renormalized parameters defined as

$$\alpha_1^* \equiv \alpha_1 + \left(\frac{2g_{11}c_{12}}{c_{11}} - 2g_{12}\right)S_x \quad \text{and} \quad \alpha_{11}^* \equiv \alpha_{11} - \frac{g_{11}^2}{2c_{11}}. \tag{2}$$

In the above, the α's are the dielectric stiffness coefficients, whereas c_{ij} and g_{ij} are the elastic stiffnesses and the electrostrictive constants, respectively. The coefficients in the Landau expansion of the free energy for PST are taken to be weighted averages of the known coefficients for bulk PTO and STO obtained from Ref. 11 and referenced therein and listed in Ref. 39. The exception is the temperature dependent $\alpha_1 = \alpha_{10}(T - T_0)$ coefficient of the P^2 term for which α_{10} and T_0 were averaged separately giving $\alpha_1(x) = (x\alpha_{10,P} + (1-x)\alpha_{10,S})(T - xT_{0,P} - (1-x)T_{0,S})$; here the subscripts P and S refer to the corresponding coefficients for PTO and STO, respectively. This form was previously shown to correctly reproduce the variation of the transition temperature with composition for bulk PST and was successfully applied to PST thin films on $DyScO_3$ substrates.[30,40] Rotations of the oxygen octahedra which are expected to be important only for the STO-rich compositions at cryogenic temperatures have not been considered in this work.

The calculated T_C as a function of composition is shown together with the experimental values in Fig. 1(b). Overall, good agreement is observed between the LD theory prediction and the experimental data despite the simplicity of the model that neglects the presence of domains which we turn to next.

To investigate the polarization distribution in our films, we resort to direct and reciprocal space measurements using ambient PFM and XRD, respectively. Direct imaging of ferroelectric domains was performed using PFM in DART mode[41] with a Cypher AFM from Asylum Research. The piezoresponse amplitude and phase images are shown in Figs. 2(a) and 2(b) for a 42-nm-thick sample with $x = 0.8$ grown directly on Nb:STO. 180° phase changes, accompanied by a drop in amplitude at the boundaries, are classic signatures of ferroelectric domains with opposite polarization orientations. As the lattice parameter of Nb:STO (3.905 Å) is smaller than the paraelectric lattice constant of the films for all compositions, the films are effectively under compressive strain[36] and we expect the polarization direction to be out-of-plane and hence only 180° domains (if any) to be present. For all PST compositions and film thicknesses investigated, the domain structure consists of bubble-like up domains embedded in a down-polarized matrix indicating the presence of an intrinsic built-in field. Such asymmetry was also reported in PTO heterostructures in a previous work.[6]

Ferroelectric 180° domains are also known to give rise to additional features in X-ray scattering measurements. For regular, periodic domain structures, distinct domain satellites are observed,[1,2] whereas less regular domain arrangements lead to broad shoulders around the Bragg peaks of the film.[4,42,43] The positions of these features in reciprocal space define a characteristic in-plane

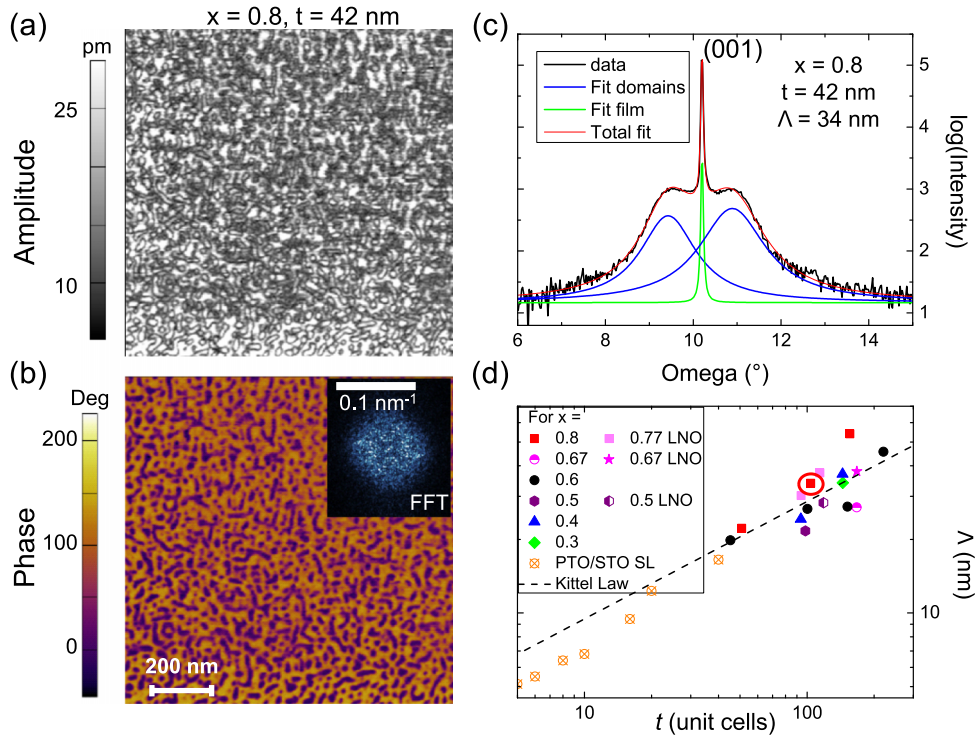

FIG. 2. Observation and analysis of intrinsic domains. (a) Amplitude and (b) phase ambient room temperature PFM images using DART mode for a 42-nm-thick sample with $x = 0.8$ grown on Nb:STO. Regions of reduced amplitude in (a) mark domain walls that separate domains of opposite polarization appearing as regions with 180° difference in PFM phase in (b). From the fast Fourier transform (inset in (b)) of the phase data, Λ is estimated to be 38 nm following the analysis in Ref. 6. (c) Incident angle omega scan (rocking curve) around the (001) film peak of the same sample. The broad satellite peaks are signatures of 180° domains with a characteristic separation Λ = 34 nm estimated from the positions of the fitted Lorentzian curves (blue). (d) Λ values obtained from rocking curve measurements for films of different thickness t and with different bottom electrodes. Data for PTO/STO superlattices (crossed orange circles) are also included.[12] For comparison, the dashed line represents the square root behavior of Kittel law. The encircled data point corresponds to the sample presented in panels (a)–(c).

length scale Λ. For a periodic system, Λ is the domain periodicity, whereas for less regular domain structures it is related to the separation between domains of the same polarization. Fig. 2(c) shows a rocking curve for the same 42-nm-thick sample with $x = 0.8$ around the (001) diffraction peak of the PST film. The main film peak and the satellites were fitted with three Lorentzian curves (green and blue lines in Fig. 2(c)) and the peak positions were used to determine Λ, which is plotted as a function of film thickness in Fig. 2(d). Λ increases with film thickness as expected for domains that form to minimize the electrostatic energy. On the same graph, the domain periodicities for PTO/STO superlattices from Ref. 12 are also shown for comparison. For SL samples with sufficiently thick STO layers, the PTO layers are electrostatically decoupled and the domain sizes are comparable to those of individual ferroelectric films of corresponding thicknesses. Within the sizable experimental scatter, all data are consistent with a square-root (Landau-Lifshitz-Kittel) dependence of the domain size on film thickness.[44,45] Using the sample tetragonality as a proxy for the magnitude of the polarization[46] reveals that domain sizes do not show any obvious dependence on the polarization, which changes by more than a factor of two from $x = 0.3$ to $x = 0.8$. Fig. 2(d) also includes data for PST films with a different bottom electrode, LNO, allowing the effects of different electrostatic boundary conditions to be probed. No significant difference in domain size is observed between films with LNO and Nb:STO bottom electrodes. By contrast, samples with (*in situ*-grown) $SrRuO_3$ bottom electrodes were observed to be monodomain, implying either that the screening at the $SrRuO_3$ interface is more efficient or that a stronger built-in field is present.[47]

TABLE I. Comparing the characteristic Λ and domain sizes d obtained by different techniques based on PFM and XRD measurements for two samples with $x = 0.8$. The error bars for the XRD and FFT are obtained from the standard error of the fits of the intensity distribution. For the real space analysis, the errors are obtained statistically. For the RAC method, they are estimated from the uncertainty in determining the positions of minima and maxima.

	Characteristic Λ			Characteristic d	
Film thickness (nm)	XRD (nm)	PFM FFT (nm)	PFM RAC (nm)	Real space analysis of PFM (nm)	PFM RAC (nm)
63	54 ± 6	56 ± 3	43 ± 4	21 ± 6	24 ± 3
42	34 ± 4	38 ± 3	31 ± 4	14 ± 7	17 ± 4

We now compare the values of Λ obtained by XRD with those obtained from real-space analysis of the PFM images and their fast Fourier transforms (FFT) (see Table I and Fig. 3). The 2D-FFTs of the PFM phase images were obtained using Gwyddion software and are displayed as insets in Fig. 3. The FFT power spectra show a ring of intensity corresponding to a real-space domain separation. Reciprocal space radial (Q) profiles were obtained by integrating the FFT data with respect to the azimuthal angle and symmetrizing the resulting profiles as described in Ref. 6. In Fig. 3(a), the obtained spectra are superimposed onto the XRD data for two samples (63 nm and 42 nm thick) with $x = 0.8$. Good agreement is observed between the two methods. The PFM phase images were also used to obtain the radial autocorrelation (RAC) function, shown in Fig. 3(c) using the method in Ref. 48. The first minimum and maximum in the normalized autocorrelation provide information on the average domain size d and spacing between like domains Λ, respectively.

Finally, we extracted the domain sizes directly by binarizing the phase images and counting the number of pixels in connected regions corresponding to individual up-polarized domains. These values were used to obtain the average effective domain diameters, which are summarized in Table I.

Despite the rather different domain configurations of both samples (as shown in Fig. 3(b), the up and down domain fractions are roughly the same for the 42-nm-thick film, while the 63-nm-thick

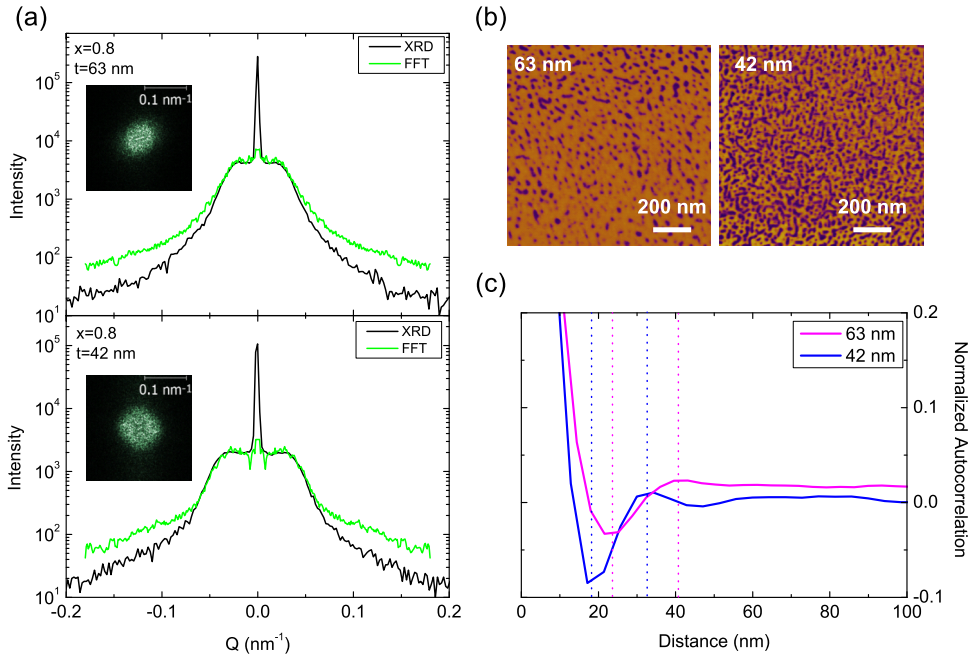

FIG. 3. Comparison of the different methods used to characterise the characteristic length scales for the domain structure. (a) XRD data superimposed on the FFT spectra calculated from the PFM data for two $x = 0.8$ samples (63 nm and 42 nm thick). (b) PFM phase images and (c) their radial autocorrelation functions.

film shows a stronger preference for one polarization and a less homogeneous distribution of oppositely polarized domains) similar conclusions can be drawn for both. In both cases reasonably good agreement is observed between the Λ values obtained by FFT and the XRD, validating XRD as a useful alternative to PFM even in cases where domains are not periodic. Although the values obtained using the two techniques are within each other's error bars, some difference may be expected due to PFM resolution being limited to ~5 nm (Ref. 49) and due to possible anisotropy in the domain structure (unlike the PFM FFT data, the XRD data are not averaged over the azimuthal angle). On the other hand, length scales obtained from the autocorrelation analysis are found to be substantially smaller. Such a discrepancy has previously been noted for ferroelectric stripe domains[4] and structural domains in manganite thin films[42] and attributed to variations in domain size or periodicity. For large variations in domain size or periodicity, the peaks in reciprocal space shift to lower Q values, leading to overestimates of the corresponding length scales calculated directly from the peak positions.

Having established how the domain sizes depend on PST composition and thickness, we next investigate the effect of the domains on the lattice parameters. The evolution of the tetragonality ratio c/a extracted from the XRD measurements is plotted in Fig. 4(a) for different compositions and film thicknesses. As the films are fully strained to the Nb:STO substrate, the in-plane lattice parameter a is taken to be the same as the cubic lattice constant of the substrate. For a fixed thickness, c/a decreases with decreasing PTO fraction, as expected from combining PTO ($a = b = 3.904$ Å, $c = 4.157$ Å in bulk) with STO ($a = b = c = 3.905$ Å in bulk).

A comparison of the composition dependence of the room temperature tetragonality with the prediction of the LD model (under the assumption of a homogeneous polarization) is shown in Fig. 4(b). The non-linear scaling of c/a with x reflects the expected strong evolution of the spontaneous polarization with composition (orange curve) as the tetragonality and polarisation P are related via $\frac{c}{a} - \left(\frac{c}{a}\right)_{para} \propto P^2$, where $\left(\frac{c}{a}\right)_{para}$ is the tetragonality of the strained film in the paraelectric phase. Comparing the experimental c/a data to the LD prediction (Fig. 4(b)) reveals better agreement for thicker samples (triangles), whereas thinner samples (circles) tend to have lower tetragonalities.

In the absence of domains, the reduced tetragonality has previously been interpreted as being due to the progressive increase in the strength of the depolarizing field for thinner films with imperfect screening of the polarization by the metallic electrodes.[46,50–52] In our case, the reduced tetragonality is likely related to the presence of the domain structure itself that can affect the lattice parameters in several ways.[10,18,19,53,54] Although the domains form to reduce the depolarizing field generated by unscreened polarization, they nevertheless do not completely eliminate it. Instead, inhomogeneous depolarizing fields are confined within a surface layer, decaying exponentially over a length scale comparable to the domain size.[10,13,14,18,19,53–55] As the domain size in our films is comparable to the film thickness, these stray fields may be expected to lead to a significant reduction of the average c-axis lattice parameter. Additionally, domain walls are regions where the polarization goes to zero and therefore favor a reduced tetragonality. Because the lattice parameter must

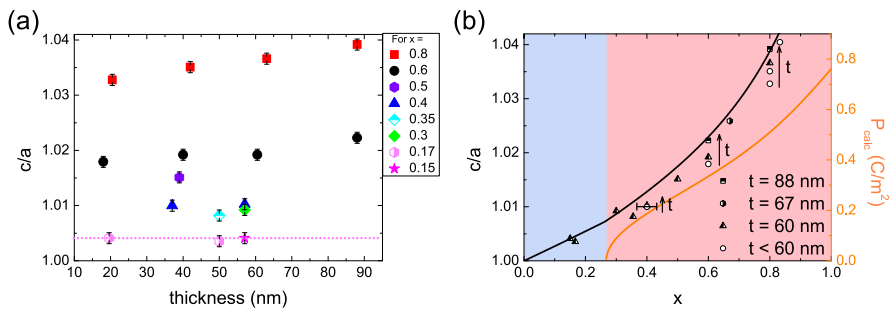

FIG. 4. (a) c/a as a function of thickness. The error bars represent the uncertainty in parameters used to simulate the data. (b) c/a for different compositions and thicknesses compared with the LD prediction (black curve), showing good agreement for the thicker samples. The orange curve shows the LD prediction for the polarization at room temperature.

be continuous across the structure laterally, the domain wall regions will compete elastically with the domains and one may expect that thinner samples with higher domain wall density will have a stronger tendency towards an overall reduction of the tetragonality. On the other hand, if a built-in field is present in our films, this should lead to an overall increase of tetragonality; its dependence on film thickness, however, is yet to be investigated. For the samples which are paraelectric at room temperature ($x = 0.17$) no thickness dependence is observed for the lattice parameter, consistent with the absence of polarization (and domains).

In summary, we have shown that by varying the composition of PST thin films, the transition temperature and lattice parameters can be tuned over a wide range of values and for thick films the behavior is well described by a simple LD model. The lower tetragonality observed in thinner films is interpreted as being due to the 180° domains that form in response to the poor screening of the ferroelectric polarization. The domain sizes in these films (few tens of nm) enable their observation by both XRD and PFM techniques, offering the possibility to compare their characteristics length scales obtained with both methods. Due to the non-periodic arrangement of the domains, the length scales obtained from reciprocal space methods were found to be larger than those found from a direct space analysis, in agreement with previous reports.[4,42]

We acknowledge Dr. Döbeli from ETH Zurich for the RBS measurements. We thank M. Lopes and S. Muller for technical support. We also thank Dr. E. Bousquet, Professor P. Paruch, I. Gaponenko, and A. Fête for valuable discussions. This work was supported by the Swiss National Science Foundation. The research leading to these results has received funding from the European Research Council under the European Union's Seventh Framework Program (No. FP7/2007-2013) ERC Grant Agreement No. 319286 (Q-MAC).

[1] S. K. Streiffer, J. A. Eastman, D. D. Fong, C. Thompson, A. Munkholm, M. V. Ramana Murty, O. Auciello, G. R. Bai, and G. B. Stephenson, Phys. Rev. Lett. **89**, 067601 (2002).
[2] D. D. Fong, G. B. Stephenson, S. K. Streiffer, J. A. Eastman, O. Auciello, P. H. Fuoss, and C. Thompson, Science **304**, 1650 (2004).
[3] V. Nagarajan, J. Junquera, J. Q. He, C. L. Jia, R. Waser, K. Lee, Y. K. Kim, S. Baik, T. Zhao, R. Ramesh, P. Ghosez, and K. M. Rabe, J. Appl. Phys. **100**, 051609 (2006).
[4] R. Takahashi, O. Dahl, E. Eberg, J. K. Grepstad, and T. Tybell, J. Appl. Phys. **104**, 064109 (2008).
[5] H. Lu, X. Liu, J. D. Burton, C.-W. Bark, Y. Wang, Y. Zhang, D. J. Kim, A. Stamm, P. Lukashev, D. A. Felker, C. M. Folkman, P. Gao, M. S. Rzchowski, X. Q. Pan, C.-B. Eom, E. Y. Tsymbal, and A. Gruverman, Adv. Mater. **24**, 1209 (2012).
[6] C. Lichtensteiger, S. Fernandez-Pena, C. Weymann, P. Zubko, and J.-M. Triscone, Nano Lett. **14**, 4205 (2014).
[7] D. D. Fong, A. M. Kolpak, J. A. Eastman, S. K. Streiffer, P. H. Fuoss, G. B. Stephenson, C. Thompson, D. M. Kim, K. J. Choi, C. B. Eom, I. Grinberg, and A. M. Rappe, Phys. Rev. Lett. **96**, 127601 (2006).
[8] A. M. Kolpak, I. Grinberg, and A. M. Rappe, Phys. Rev. Lett. **98**, 166101 (2007).
[9] R. Takahashi, J. K. Grepstad, T. Tybell, and Y. Matsumoto, Appl. Phys. Lett. **92**, 112901 (2008).
[10] M. J. Highland, T. T. Fister, M.-I. Richard, D. D. Fong, P. H. Fuoss, C. Thompson, J. A. Eastman, S. K. Streiffer, and G. B. Stephenson, Phys. Rev. Lett. **105**, 167601 (2010).
[11] M. Dawber, N. Stucki, C. Lichtensteiger, S. Gariglio, P. Ghosez, and J.-M. Triscone, Adv. Mater. **19**, 4153 (2007).
[12] P. Zubko, N. Jecklin, A. Torres-Pardo, P. Aguado-Puente, A. Gloter, C. Lichtensteiger, J. Junquera, O. Stephan, and J.-M. Triscone, Nano Lett. **12**, 2846 (2012).
[13] Y. L. Tang, Y. L. Zhu, X. L. Ma, A. Y. Borisevich, A. N. Morozovska, E. A. Eliseev, W. Y. Wang, Y. J. Wang, Y. B. Xu, Z. D. Zhang, and S. J. Pennycook, Science **348**, 547 (2015).
[14] A. K. Yadav, C. T. Nelson, S. L. Hsu, Z. Hong, J. D. Clarkson, C. M. Schlepuetz, A. R. Damodaran, P. Shafer, E. Arenholz, L. R. Dedon, D. Chen, A. Vishwanath, A. M. Minor, L. Q. Chen, J. F. Scott, L. W. Martin, and R. Ramesh, Nature **530**, 198 (2016).
[15] P. Zubko, N. Stucki, C. Lichtensteiger, and J.-M. Triscone, Phys. Rev. Lett. **104**, 187601 (2010).
[16] J. Y. Jo, P. Chen, R. J. Sichel, S. J. Callori, J. Sinsheimer, E. M. Dufresne, M. Dawber, and P. G. Evans, Phys. Rev. Lett. **107**, 055501 (2011).
[17] V. A. Stephanovich, I. A. Luk'yanchuk, and M. G. Karkut, Phys. Rev. Lett. **94**, 047601 (2005).
[18] I. A. Luk'yanchuk, L. Lahoche, and A. Sené, Phys. Rev. Lett. **102**, 147601 (2009).
[19] S. Prosandeev and L. Bellaiche, Phys. Rev. B **75**, 172109 (2007).
[20] P. Aguado-Puente and J. Junquera, Phys. Rev. Lett. **100**, 177601 (2008).
[21] S. Lisenkov, I. Ponomareva, and L. Bellaiche, Phys. Rev. B **79**, 024101 (2009).
[22] Q. Zhang, R. Herchig, and I. Ponomareva, Phys. Rev. Lett. **107**, 177601 (2011).
[23] E. Glazkova, K. McCash, C.-M. Chang, B. K. Mani, and I. Ponomareva, Appl. Phys. Lett. **104**, 012909 (2014).
[24] G. Catalan, J. Seidel, R. Ramesh, and J. F. Scott, Rev. Mod. Phys. **84**, 119 (2012).
[25] C. Thompson, D. D. Fong, R. V. Wang, F. Jiang, S. K. Streiffer, K. Latifi, J. A. Eastman, P. H. Fuoss, and G. B. Stephenson, Appl. Phys. Lett. **93**, 182901 (2008).
[26] S. Nomura and S. Sawasa, J. Phys. Soc. Jpn. **10**, 108 (1954).
[27] V. V. Lemanov, E. P. Smirnova, and E. A. Tarakanov, Phys. Solid State **39**, 628 (1997).

[28] Y. Somiya, A. S. Bhalla, and L. Cross, Int. J. Inorg. Mater. **3**, 709 (2001).
[29] X. Xing, J. Chen, J. Deng, and G. Liu, J. Alloys Compd. **360**, 286 (2003).
[30] G. Rispens, J. Heuver, and B. Noheda, Appl. Phys. Lett. **97**, 262901 (2010).
[31] S. Matzen, O. Nesterov, G. Rispens, J. A. Heuver, M. Biegalski, H. M. Christen, and B. Noheda, Nat. Commun. **5**, 4415 (2014).
[32] For PST, optimal growth conditions were found to be at a total pressure of 180 mTorr with an oxygen/argon mixture of 20:29 and a substrate temperature of 540 °C. For LNO, the previously reported conditions in Ref. 56 were the one used.
[33] C. Lichtensteiger, "Ferroelectricity at the nanoscale: Study of size effects in lead titanate thin films," Ph.D. thesis, University of Geneva, 2006.
[34] E. D. Specht, H.-M. Christen, D. P. Norton, and L. A. Boatner, Phys. Rev. Lett. **80**, 4317 (1998).
[35] K. J. Choi, M. Biegalski, Y. L. Li, A. Sharan, J. Schubert, R. Uecker, P. Reiche, Y. B. Chen, X. Q. Pan, V. Gopalan, L.-Q. Chen, D. G. Schlom, and C. B. Eom, Science **306**, 1005 (2004).
[36] N. A. Pertsev, A. G. Zembilgotov, and A. K. Tagantsev, Phys. Rev. Lett. **80**, 1988 (1998).
[37] N. A. Pertsev, A. G. Zembilgotov, and A. K. Tagantsev, Ferroelectrics **223**, 79 (1999).
[38] N. A. Pertsev, A. K. Tagantsev, and N. Setter, Phys. Rev. B **61**, R825 (2000).
[39] All values are given in SI units (a_1 = JmC^{-2}, a_{11} = Jm^{5}C^{-4}, a_{111} = Jm^{9}C^{-6}, g_{ij} = JmC^{-2}, c_{ij} = Jm^{-3}). For $PbTiO_3$: $a_1 = 3.8 \times 10^5(T - 752)$, $a_{11} = 4.229 \times 10^8$, $a_{111} = 2.6 \times 10^8$, $c_{11} = 1.746 \times 10^{11}$, $c_{12} = 0.794 \times 10^{11}$, $g_{11} = 1.14 \times 10^{10}$, $g_{12} = 4.63 \times 10^8$. For $SrTiO_3$: $a_1 = 7.45 \times 10^5(T - 51.64)$ (This is a linear approximation that is only valid above ≈100 K), $a_{11} = 2.02 \times 10^9$, $c_{11} = 3.36 \times 10^{11}$, $c_{12} = 1.07 \times 10^{11}$, $g_{11} = 1.25 \times 10^{10}$, $g_{12} = -0.108 \times 10^{10}$.
[40] G. Rispens, "Strain and composition effects in epitaxial ferroelectrics—Structural studies on $Pb_xSr_{1-x}TiO_3$ thin films grown by MBE," Ph.D. thesis, University of Groningen, 2010.
[41] A. Gannepalli, D. G. Yablon, A. H. Tsou, and R. Proksch, Nanotechnology **22**, 355705 (2011).
[42] G. Carbone, Ph.D. thesis, Institut für Theoretishe und Angewandte Physik der Universität Stuttgart, 2004.
[43] R. V. Wang, D. D. Fong, F. Jiang, M. J. Highland, P. H. Fuoss, C. Thompson, A. M. Kolpak, J. A. Eastman, S. K. Streiffer, A. M. Rappe, and G. B. Stephenson, Phys. Rev. Lett. **102**, 047601 (2009).
[44] L. Landau and E. Lifshitz, Phys. Z. Sowjetunion **8**, 153–169 (1935).
[45] C. Kittel, Solid State Commun. **10**, 119 (1972).
[46] C. Lichtensteiger, J.-M. Triscone, J. Junquera, and P. Ghosez, Phys. Rev. Lett. **94**, 047603 (2005).
[47] A. Kopal, P. Mokry, J. Fousek, and T. Bahnik, Ferroelectrics **223**, 127 (1999).
[48] See http://imagejdocu.tudor.lu/doku.php?idmacro:radially_averaged_autocorrelation for the software used is ImageJ with the autocorrelation function macro.
[49] C. Blaser and P. Paruch, New J. Phys. **17**, 013002 (2015).
[50] I. Batra and B. D. Silverman, Solid State Commun. **11**, 291 (1972).
[51] R. R. Mehta, B. D. Silverman, and J. T. Jacobs, J. Appl. Phys. **44**, 3379 (1973).
[52] M. Glinchuk, E. Eliseev, and V. A. Stephanovich, Physica B **322**, 356 (2002).
[53] I. Kornev, H. Fu, and L. Bellaiche, Phys. Rev. Lett. **93**, 196104 (2004).
[54] F. D. Guerville, I. Luk'yanchuk, L. Lahoche, and M. E. Marssi, Mater. Sci. Eng., B **120**, 16 (2005).
[55] C. Lichtensteiger, P. Zubko, M. Stengel, P. Aguado-Puente, J.-M. Triscone, P. Ghosez, and J. Junquera, in *Oxide Ultrathin Films: Science and Technology*, edited by G. Pacchioni and S. Valeri (Wiley, New York, 2011), Chap. 12.
[56] R. Scherwitzl, P. Zubko, C. Lichtensteiger, and J.-M. Triscone, Appl. Phys. Lett. **95**, 222114 (2009).